Fuel 407 (2026) 137369

Contents lists available at ScienceDirect

Fuel

journal homepage: www.elsevier.com/locate/fuel

Full Length Article

Ignition characteristics of flowing ammonia-containing mixtures with nanosecond pulsed discharges

Bowen Liu [a,b,1], Xiaoyang Guo [a,1], Zihao Chen [a], Erjiang Hu [a,*], Hao Zhao [b], Zuohua Huang [a]

[a] State Key Laboratory of Multiphase Flow in Power Engineering, Xi'an Jiaotong University, Xi'an 710049, China
[b] School of Mechanics and Engineering Science, Peking University, Beijing 100871, China

ARTICLE INFO

Keywords:
Minimum ignition energy (*MIE*)
Ammonia
Flowing ignition
Flame kernel propagation
Nanosecond pulsed discharges

ABSTRACT

The ignition and flame propagation characteristics of ammonia-containing mixtures under flowing conditions were investigated using a mini-wind tunnel combustion chamber coupled with nanosecond pulsed discharges. The ignition probability and minimum ignition energy (*MIE*) for flowing ammonia (NH_3)/air and NH_3/ethylene (C_2H_4)/air mixtures were measured, evaluating the effects of equivalence ratios, fuel compositions, flow velocities, and discharge parameters through experimental measurements and data analysis. The *MIE* of NH_3/air mixtures varied non-monotonically with the equivalence ratio, reaching a minimum near an equivalence ratio of 0.85. The flame kernel area and chemiluminescence intensities of NH_3/air flames also showed a tendency to increase and then decrease as the equivalence ratio increased on the lean side. For NH_3/C_2H_4/air mixtures, higher flow velocities and greater ammonia fractions increased the *MIE* due to enhanced convective heat losses and reduced chemical reactivity. The flame propagation process was divided into four stages: ignition, quasi-steady-state development, wall-touch propagation, and outflow. In the fully coupled state, at lower discharge frequencies and larger pulse numbers, flame kernel growth was significantly enhanced. However, a saturation point was reached beyond which additional pulses or increasing frequencies did not notably change the kernel size. This study provides critical insights into plasma-assisted ignition and flame propagation under flowing conditions for ammonia-containing fuels, contributing to the advancement of low-carbon combustion technologies.

1. Introduction

The combustion of fossil fuels has led to severe atmospheric pollution, global warming, and climate change [1]. To achieve sustainable and low-carbon energy conversion, various alternative fuels such as biomass [2], hydrogen (H_2) [3–5], and ammonia (NH_3) [6], which has been used industrially for over a century, benefits from a well-established infrastructure for production, storage, and transportation [7]. However, its practical application as a fuel is hindered by high NOx emissions [8], low burning intensity [9–11], and a large minimum ignition energy (*MIE*) [9]. While two-stage stratified combustion has been shown to reduce NOx emissions [12], and blending with more reactive species (such as H_2 [3–5,8,13], CH_4 [14], C_2H_4 [15], DME [16,17], CH_3OH [18], and others.) can enhance flame intensity, NH_3/air still exhibits a significantly higher *MIE* (about 680 mJ) [13] under atmospheric conditions. The *MIE* of NH_3/air is several orders of magnitude higher than CH_4/air (about 0.47 mJ) and H_2/air (about 0.02 mJ) mixtures.

Numerous studies have characterized the flammability limits, ignition energies, and burning velocities of NH_3-containing mixtures [9,19–24]. For instance, Pfahl et al. [9] investigated the flammability limit, ignition energy and the burning velocity of the H_2-CH_4-NH_3-N_2O-O_2-N_2 mixture. Their results demonstrated that a static NH_3/air mixture (21.9 % NH_3, 78.1 % air) under an initial pressure of 100 kPa and stoichiometric ratio could not be ignited with an energy of less than 50 mJ, but was combustible with ignition energies greater than 100 mJ. Sadaghiani et al. [24] measured the *MIE* of NH_3/air mixtures, and found that the *MIE* was 18 mJ at an equivalence ratio of 0.9. They also found that the *MIE* was influenced by the mixture composition, temperature, pressure, spark gap, spark duration, and the electrode geometry.

* Corresponding author.
E-mail address: hujiang@xjtu.edu.cn (E. Hu).
[1] These authors contributed to the work equally and should be regarded as co-first authors.

https://doi.org/10.1016/j.fuel.2025.137369
Received 7 September 2025; Received in revised form 14 October 2025; Accepted 28 October 2025
Available online 31 October 2025

Lesmana et al. [19] examined the effect of ignition gap and duration on the *MIE* of partially dissociated NH_3. At a fixed ignition gap and equivalence ratio, the *MIE* decreased with increasing dissociation of NH_3, primarily due to the higher reactivity of H_2 released from the NH_3 dissociation process. For NH_3/air flames, the minimum *MIE* occurred near an equivalence ratio of 0.9, which aligns with the results obtained by Sadaghiani et al. [20]. However, the majority of these fundamental investigations have been conducted under quiescent or low-velocity flow conditions. In practical combustion systems, including internal engines, gas turbines, and industrial burners [25], the fuel/air mixture invariably flows at high velocities and is often turbulent (mean velocities >10 m/s). Despite this, there is a notable lack of experimental data on ignition characteristics for high-velocity flowing ammonia-containing mixtures.

High-voltage nanosecond pulsed discharges have emerged as a promising ignition technology capable of depositing the required energy in extremely short times and generating non-equilibrium plasma to facilitate rapid kernel formation [26–36]. Building on this, recent plasma-assisted combustion research has emphasized kinetic enhancements in challenging fuel [37–39]. Several studies have explored nanosecond pulsed discharge ignition of flowing hydrocarbon or H_2-containing mixtures [28,29,35,36,40,41]. Ombrello et al. [42] demonstrated that nanosecond pulsed high-frequency discharges at higher than 5 kHz significantly broadened the ethylene cavity ignition range in Mach flows, reducing energy requirements and improving ignition probability and speed through enhanced pulse synergy. Lefkowitz et al. [36] identified three inter-pulse coupling regimes, including full coupling, partial coupling, and decoupling, each exhibiting distinct ignition probabilities and flame-kernel morphologies as a function of discharge frequency. Opacich et al. [29] demonstrated that, at equal maximum average power, nanosecond pulsed-repetitive discharges yield substantially larger ignition kernels than conventional DC discharges. Adams et al. [31] used optical emission spectroscopy during nanosecond pin-to-pin discharges to demonstrate thermal coupling above 10 kHz, observing temperature rises of several thousand kelvin between pulses separated by less than 100 μs. Bonebrake et al. [35] further showed that, following ignition by pulsed-repetitive nanosecond discharges, both the peak temperature and initial heating rate of the flame kernels increase with discharge frequency. In summary, previous studies on the ignition of flowing mixtures using nanosecond pulsed discharges have mainly focused on the effect of discharge parameters on ignition characteristics. However, the systematic measurement of ignition probability, *MIE*, and flame-kernel dynamics for ammonia-containing flows remain unreported.

Therefore, this work aims to elucidate the ignition characteristics of high-*MIE* ammonia-containing mixtures under flowing conditions using a mini-wind tunnel combustion chamber equipped with nanosecond pulsed discharges. The ignition probability and *MIE* of flowing ammonia-containing mixtures, including NH_3/air and NH_3/C_2H_4/air, are quantified. Additionally, the effects of flow velocity, equivalence ratio, and fuel composition on the *MIE*, flame kernel development, and chemiluminescence intensity are systematically investigated. Finally, the effects of discharge parameters, such as the discharge frequency and number of pulses on flame kernel growth are analyzed.

2. Methods

2.1. Experimental methods

The ignition characteristics of premixed NH_3/C_2H_4/air flows were investigated in a mini-wind-tunnel combustion chamber coupled with a high-voltage nanosecond pulsed discharge system, as depicted in Fig. 1. The main subsystems include the advection combustion chamber, the fuel/air feed system, the discharge system, and the data acquisition system. The combustion chamber, constructed with stainless steel walls, has a radial cross-section of 4 cm × 4 cm. To ensure a uniform inlet stream and minimize flow inhomogeneities that can affect flame kernel formation and propagation, three flow-straightening orifice plates are mounted upstream, spaced 1 cm apart. These plates have a hole diameter of 2.5 mm and consist of 136, 136, and 144 holes, respectively. At the exit of the combustion chamber, an inert purge flow is introduced to prevent flame propagation. Two quartz windows are mounted on the side of the combustion chamber with a span of 20 cm × 4 cm. Illumination is provided by an LED spot lamp, collimated through a slit and two plano-convex lenses (focal length of the lens is 60 cm). The cross-sectional area of the parallel optical path covers the entire field of the window. A high-speed camera (Phantom V2012) with a resolution of 768 × 480 pixels records ignition and flame-kernel propagation. For pure NH_3/air flames, characterized by strong self-luminescence, and were captured directly at a sampling frequency of 1800 fps and an exposure time of 500 μs, while ethylene-containing flames were imaged by schlieren method with a fixed sampling frequency of 10,000 fps and the exposure time of 2.5 μs. The fuel and air flow rates were controlled by calibrated mass flow controllers (ALICAT, MCR-Series) with flow rate ranges of 0–20 L/min for NH_3, 0–100 L/min for C_2H_4, and 0–1500 L/min for air, with fuel gas purity exceeding 99.999 %. Two tungsten electrodes with a diameter of 1.5 mm were used for ignition. The tips of the tungsten electrodes were specially machined with a taper angle of 20° and were installed 20 cm downstream of the inlet of the combustion chamber in a pin-to-pin arrangement. Insulated PTFE mounts allow

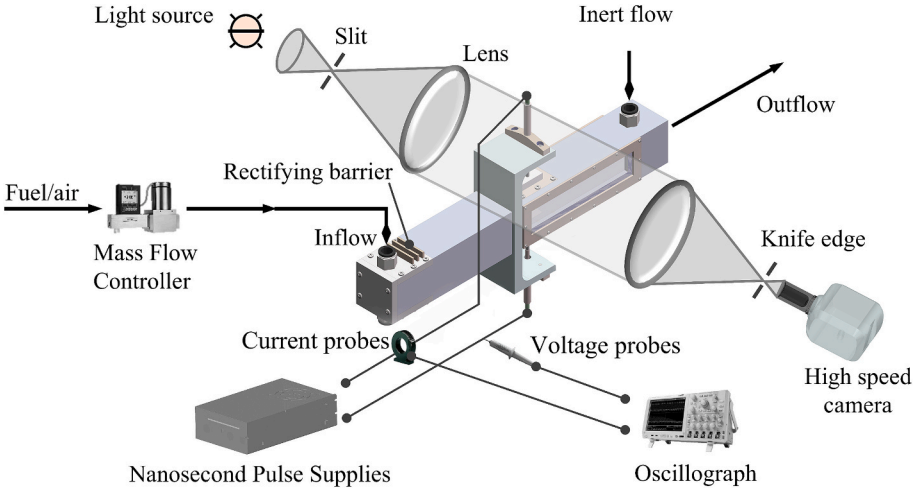

Fig. 1. Experimental setup.

manual adjustment of the electrode gap, which was kept constant at 2 mm in this study.

The ignition system employed a high-voltage nanosecond pulsed supply with adjustable output voltage (U), frequency (f), pulse width (W) and number of pulses (N). Variations in discharge energy were primarily achieved by changing the number of pulses and the voltage (10–13 kV). Lefkowitz et al. [36] studied the inter-pulse coupling process by changing the discharge frequency, identifying three modes with increasing pulse frequency: decoupled, partially coupled, and fully coupled. Their results indicated that the fully coupled mode most effectively promotes successful ignition. To minimize the influence of the coupling mode on the flow ignition characteristics, all ignition experiments were performed in a fully coupled mode by a fixed discharge frequency (f = 20 k Hz), and the discharge energy was deposited in a single kernel. Voltage and current waveforms were captured through a voltage probe (Tectronix, P6015A) and a current transformer (Pearson Electronics, 6600), respectively, and recorded on an oscilloscope (Tectronix, DPO4104B) for energy calculations. Synchronization of the pulse generator (DG535), oscilloscope capture, and high-speed imaging was achieved through a digital delay pulse generator.

2.2. Experimental conditions

All ignition tests were conducted at 293 K and 98 kPa with variations maintained within ±2 K for temperature and ±1 kPa for pressure. The *MIE* and ignition probability (P_{ig}) of the NH_3/C_2H_4/air premixed flows were measured under high-turbulence conditions, with the exception of pure NH_3/air flames, which were limited by the fuel-flow constraints. The effects of NH_3/C_2H_4 blending radio, initial flow velocity (V), and equivalence ratios (ϕ) were systematically investigated, as depicted in Table 1.

The equivalence ratio can be calculated by the following equation:

$$\phi = \frac{\left(N_{air}/N_{fuel}\right)_{stoichiometric}}{\left(N_{air}/N_{fuel}\right)_{actual}} \quad (1)$$

where N_{fuel} and N_{air} represent the mole fraction of fuel and air, respectively. V is defined as the ratio of the total volume flow rate to the inlet cross-sectional area, as follows:

$$V = \frac{Q_{in}}{A_{in}} \quad (2)$$

where Q_{in} represents the total volume flow rate, A_{in} represents the inlet cross-sectional area.

2.3. Methods of data processing

Based on the synchronized measured voltage (U) and current (I) signals, the discharge power (P) and energy deposition in single pulse discharges (E) can be calculated by Eqs. (3) and (4), respectively.

Table 1
Experimental conditions in present study.

Mixtures	Temperature (K)	Pressure (kPa)	V (m/s)	ϕ
NH_3	293	98	1	0.7, 0.8, 0.9, 1
C_2H_4			10	0.5
20 %NH_3/80 % C_2H_4			7	0.5
20 %NH_3/80 % C_2H_4			10	0.47, 0.5, 0.53
20 %NH_3/80 % C_2H_4			13	0.5
40 %NH_3/60 % C_2H_4			10	0.5

$$P = U \cdot I \quad (3)$$

$$E = \int P \cdot dt \quad (4)$$

Fig. 2 (a) shows that, for 20 %NH_3/80 %C_2H_4/air at ϕ = 0.5 and V = 10 m/s with f = 20 kHz and U_{peak} = 10 kV (the peak voltage), the energy deposition of single pulse is about 7 mJ. The voltage peaks around 50 ns after breakdown, coincident with a rapid current rise, and both signals decay thereafter. Over 90 % of the energy is deposited within the first 0.3 μs, beyond which residual oscillations arise from electromagnetic inductance. It should be noted that the measured current is the sum of the displacement current (I_{disp}) of capacitive charging from the electrodes and the conduction current streaming through the plasma. To measure I_{disp}, we reduce the discharge voltage so that the discharge process does not generate a spark, then only I_{disp} is recorded, and the relationship between I_{disp} and U can be calculated as follows:

$$I_{disp} = C\frac{dU}{dt} \quad (5)$$

where C is the equivalent capacitance. The measured total current lagged by 1.3 ns by comparing the derivative of voltage with time and the actual measured total current, thus the delay between the voltage and current probes was 1.3 ns. I was corrected by I_{disp} and the recalculated E was almost the same as the E before correction. Consequently, the effect of I_{disp} can be neglected for this work.

The total multi-pulse discharge energy was calculated by summing the individual single-pulse energies, which themselves vary with fuel reactivity and flow conditions. Fig. 2 (b) presents the statistical distributions of a 10 repeated multi-pulse discharge under three different conditions with discharge parameters of 13 kV, 20 k Hz, and pulse width of 10 ns. The results indicate that the single pulse discharge energy varies with the fuel reactivity as well as the initial flow parameters. As the V increases, the mean single-pulse energy E decreases slightly. Moreover, at lower V, pure NH_3 produces higher E than the NH_3/C_2H_4 blend at higher V. Notably, the first three pulses exhibit larger shot-to-shot E variability, with the first pulse delivering the least E and the second pulse the most; thereafter, pulse-to-pulse E stabilizes around a consistent mean.

Fig. 3 illustrates representative examples of successful and failed ignitions in pure NH_3/air flames at ϕ = 1 and V = 1 m/s. In both cases, the nanosecond pulsed discharge first produces a purple plasma glow. In the successful case (left), an initial orange-red kernel appears immediately after breakdown, then enlarges and intensifies as it transports downstream. In the failed case (right), the brightness of nascent kernel diminishes over time until it extinguishes. The schlieren-based criteria for ethylene-containing flames follow the same principle: growing, persistent kernels indicate success, whereas decaying or vanishing structures indicate failure.

The outcome of individual ignition trials is inherently stochastic, owing to heat losses, local flow inhomogeneities, and discharge-process fluctuations. To quantify ignition difficulty for a given mixture and energy level, we define the ignition probability (P_{ig}) as:

$$P_{ig} = \frac{n_{success}}{n_{total}} \times 100\% \quad (6)$$

where $n_{success}$ represents the number of successful ignitions, and n_{total} represents the total number of ignition trials. As P_{ig} is a statistical metric, a large number of repetitions is required for reliable estimation. Fig. 4 presents P_{ig} versus the number of trials for NH_3/air flames at different ignition energies under fixed flow conditions. When the trial count is limited, P_{ig} exhibits wide fluctuations, reflecting the strong influence of randomness. As more ignitions are performed, P_{ig} rapidly converges and its variability diminishes, approaching a stable value. In this work, we conducted over 60 repetitions for every condition to ensure that the

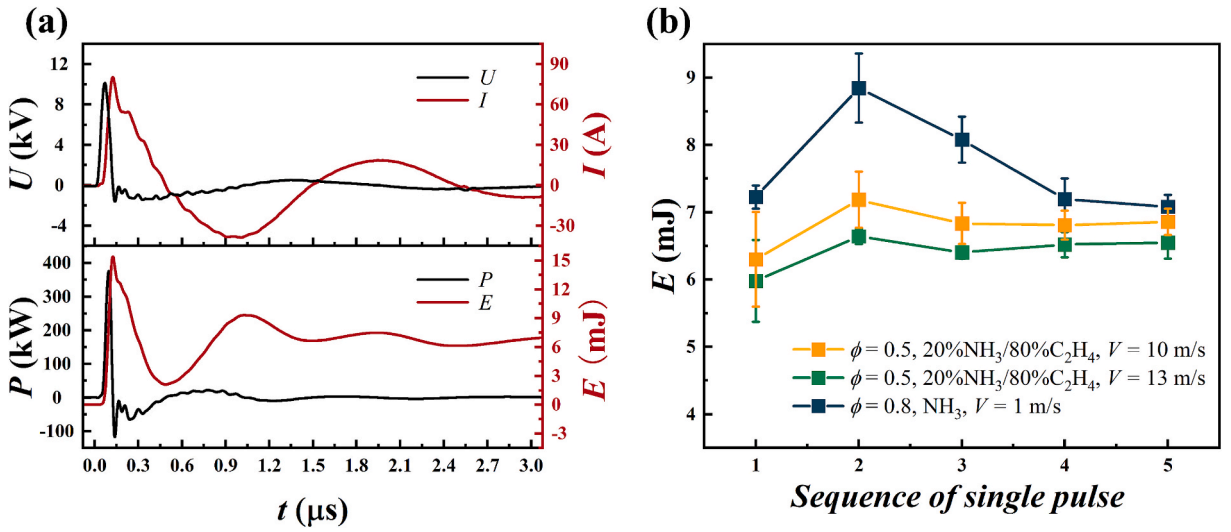

Fig. 2. Single-pulse energy deposition. (a) Representative voltage, current, power, and cumulative energy traces for a 10 kV, 20 kHz single-pulse discharge in 20 % NH_3/80 %C_2H_4/air flows at $\phi = 0.5$ and $V = 10$ m/s; (b) Variations of single pulse energy with the sequence of single pulse under different conditions.

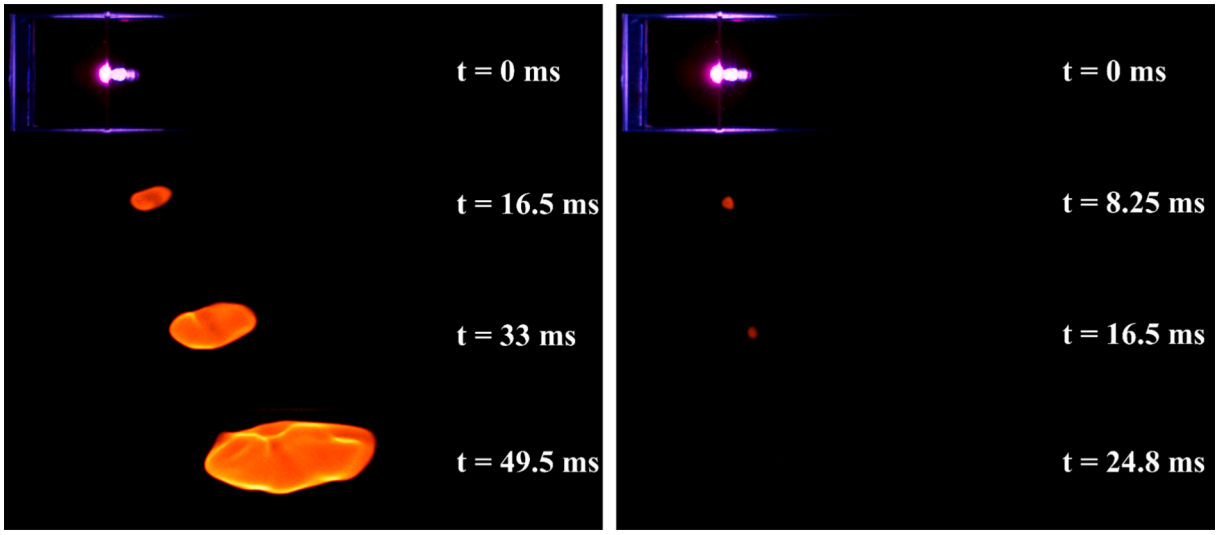

Fig. 3. Direct images of NH_3/air flames during the ignition process at $\phi = 1$, $V = 1$ m/s. The left and right images are ignition success and ignition failure cases, respectively.

reported ignition probabilities are both stable and statistically robust.

The deposited energy E and the ignition probability P_{ig} were each fitted to a lognormal cumulative distribution function [43], as follows:

$$F_{\log}(E) = \frac{1}{2}\left(1 + \mathrm{erf}\left(\frac{\ln(E) - \mu}{\sqrt{2}\sigma}\right)\right) \tag{7}$$

where μ and σ are the mean and standard deviation of the natural logarithm of the variable, respectively. It is clarified that the 95 % confidence intervals for the fitted curves are given in this work which are meaningless when $P_{ig} > 1$ or $P_{ig} < 0$. Besides P_{ig}, the *MIE* is commonly used to quantify the mixture ignitability. Here, we define the *MIE* as the ignition energy at which $P_{ig} = 50$ % [44].

An image-processing algorithm was implemented to identify flame boundaries and extract kernel areas, as depicted in Fig. 5. Within each interrogation window of known dimensions (length $a = 20$ cm, width $b = 4$ cm), so that the window area can be calculated as follows:

$$S_1 = a \cdot b \tag{8}$$

Then, the area of flame kernels can be calculated by Eq. (9). The area of flame kernels is the statistical result of >10 times repeated experiments under the target condition.

$$Area = \frac{\text{The number of recognized pixel points within the flame boundary}}{\text{The number of pixels in the window}} \cdot S_1 \tag{9}$$

3. Results and discussion

3.1. Analysis of the stages of flame kernels development

The entire ignition and flame-kernel evolution process can be divided into four distinct stages (Fig. 6): (i) the ignition stage; (ii) the quasi-steady-state development stage; (iii) the wall-touching propagation stage; and (iv) the outflow stage. Although these stages are generally similar across different mixtures, we here use pure NH_3/air at $\phi = 0.47$ and $V = 1$ m/s as an illustrative example.

Ignition stage (i): Immediately following the nanosecond breakdown, the gas between the electrode gap is excited into a plasma, emitting a characteristic purple glow. This plasma emission transiently

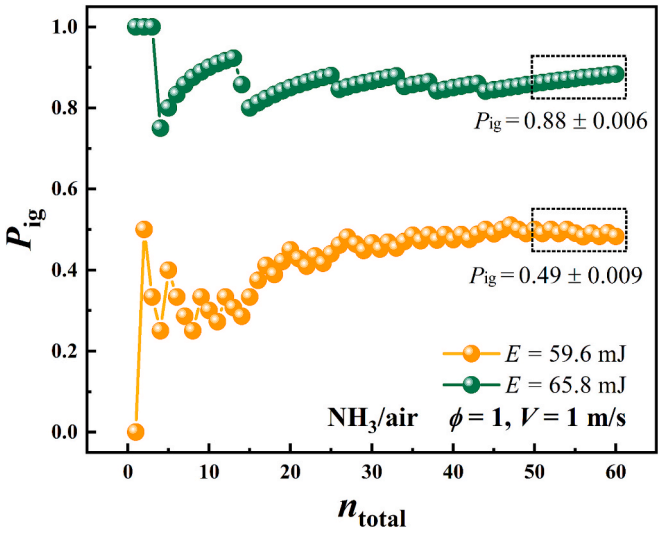

Fig. 4. Variations of the ignition probability with the number of total ignitions for NH_3/air flames under different ignition energies at $\phi = 1$, $V = 1$ m/s.

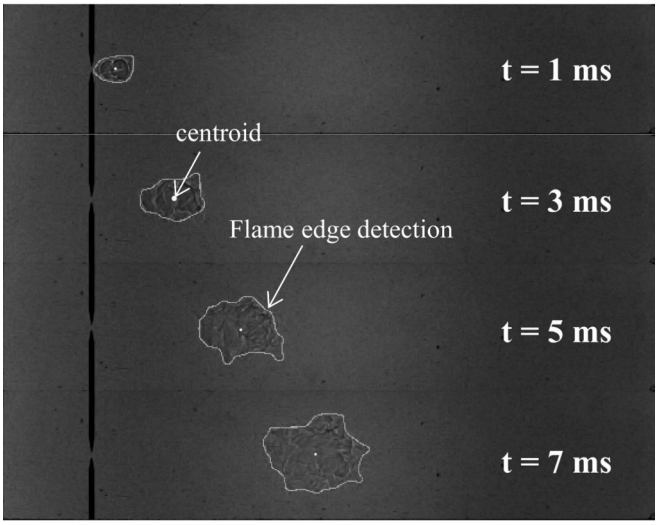

Fig. 5. Flame boundary recognition for schlieren images.

dominates the nascent flame kernel luminosity, marking the spark event.

Quasi-steady-state development stage (ii): A small orange-red kernel then emerges and advects downstream with the flow. For $t < 20$ ms after discharge, the surface area of kernel and its heat release rate are limited by its initially small flame front surface, resulting in slow growth. As the kernel enlarges, its area increases more rapidly, though still under conditions unaffected by the chamber walls.

Wall-touching propagation stage (iii): Once the expanding kernel contacts the inner wall, its growth accelerates markedly. Notably, the downstream expansion outpaces upstream propagation, since upstream movement is moderated by the balance between the incoming flow velocity and the flame burning velocity (i.e., flashback dynamics).

Outflow stage (iv): When the flame front passes beyond the outlet, the kernel convects out of the chamber. Beyond this point, the rates of area growth and luminosity both decline until the flame is fully blown out.

3.2. Ignition characterization

3.2.1. Ignition characterization for NH_3/air mixture

Fig. 7 (a) depicts the variations of the P_{ig} of NH_3/air mixtures with ignition energy for different equivalence ratios. On the lean side, a non-monotonic dependence of P_{ig} on ϕ is revealed, in contrast to other basic combustion characteristics. As ϕ is increased from 0.7 to 0.8, the P_{ig} curves are shifted leftward, indicating a reduction in the *MIE* and hence an easing of ignition. However, upon further enrichment to $\phi = 1$, a rightward shift is observed, signifying increased ignition difficulty. In particular, the *MIE* is found to rise to 59.2 mJ at $\phi = 1$, which nearly double the value measured at $\phi = 0.8$. Fig. 7 (b) more clearly illustrates the relationship between ϕ and *MIE* on the lean side. Under the flowing conditions, a quadratic fit of the experimental data suggests that the *MIE* decreases with increasing ϕ up to approximately 0.85, beyond which it increases again, exhibiting a pronounced U-shaped trend. Based on this fitting, it is inferred that the optimal ignitability of NH_3/air mixtures in the tested configuration likely occurs at an equivalence ratio near $\phi = 0.85$.

3.2.2. Ignition characterization for NH_3/C_2H_4/air mixture

In this work, the effects of the fuel compositions, equivalence radio (ϕ), and flow velocity (V) on ignition characteristics are explored for NH_3/C_2H_4/air flames. Fig. 8 (a) depicts the variations of P_{ig} with E for NH_3/C_2H_4/air mixtures at $V = 10$ m/s and $\phi = 0.5$ for three different fuel compositions. The fuel composition likewise governs the reactivity of the mixture. As NH_3 is intrinsically less reactive, increasing its blending ratio progressively lowers the overall mixture reactivity. With the NH_3 fraction rising, the P_{ig} curves shift to higher energies and the *MIE* increases, directly reflecting the diminished reactivity of the

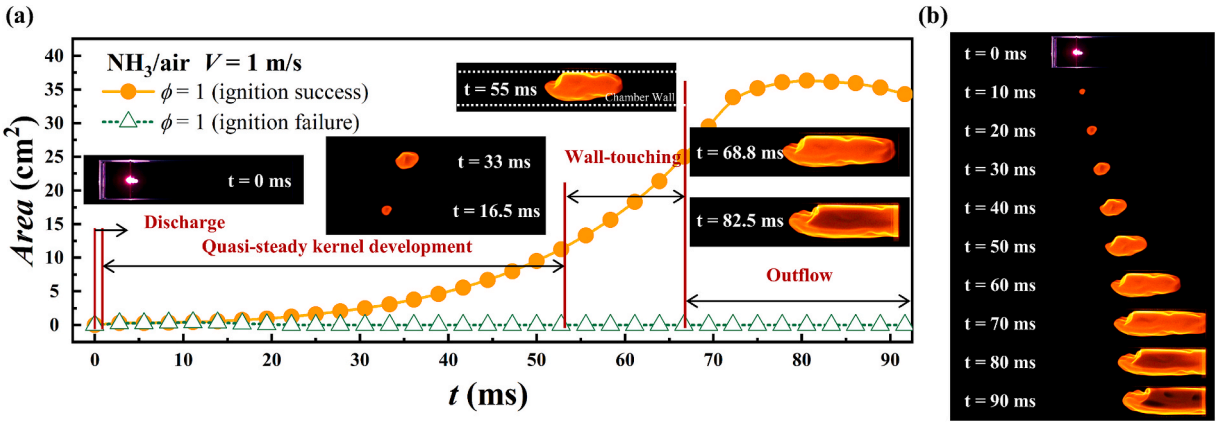

Fig. 6. Stages of development of NH_3/air flame kernels under $V = 1$ m/s, $\phi = 1$. (a) Variations of the flame area of NH_3/air with time; (b) Photographs of NH_3/air flame at different times.

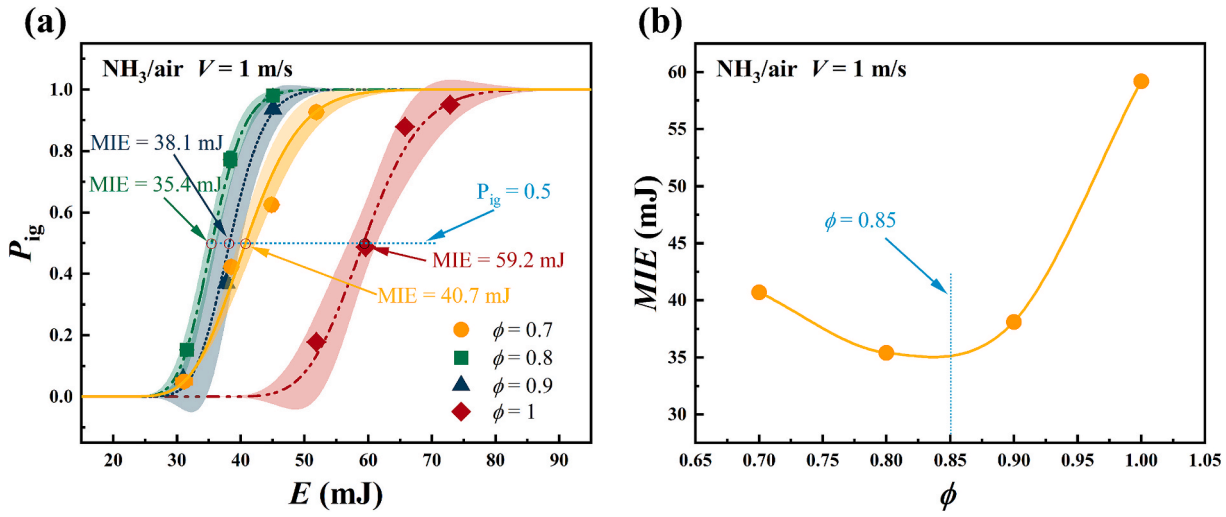

Fig. 7. Ignition characteristics of NH_3/air mixtures under $V = 1$ m/s at different equivalence ratios. (a) Variations of the ignition probability with ignition energy; (b) Variations of the minimum ignition energy with equivalence ratios.

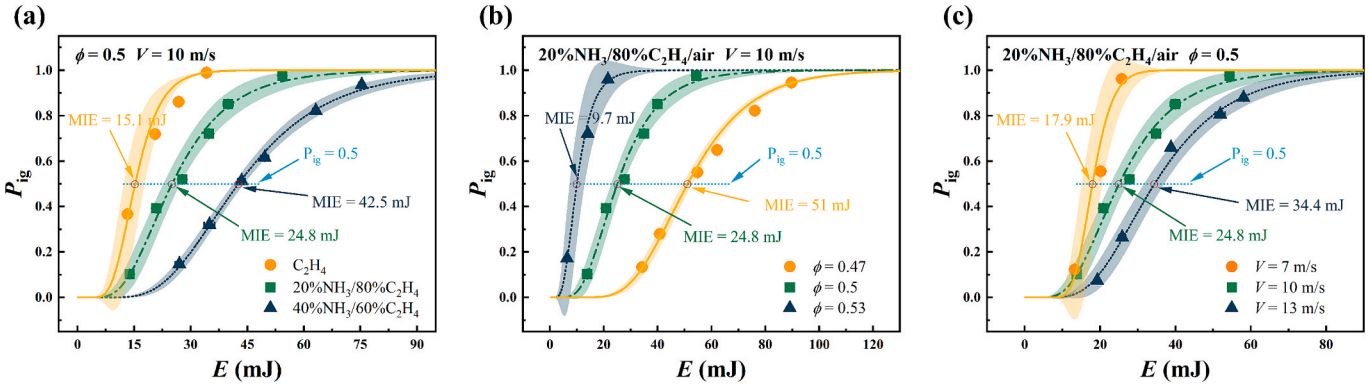

Fig. 8. Ignition characteristics of NH_3/C_2H_4/air mixtures under different conditions. (a) Variations of the ignition probability with ignition energy for NH_3/C_2H_4/air flames under $V = 10$ m/s and $\phi = 0.5$ with different fuel compositions; (b) Variations of the ignition probability with ignition energy for 20 %NH_3/80 %C_2H_4/air mixtures under $V = 10$ m/s at different equivalence ratios. (c) Variations of the ignition probability with ignition energy for 20 %NH_3/80 %C_2H_4/air mixtures at $\phi = 0.5$ under different initial flow velocities.

mixture. A low-reactivity mixture releases heat more slowly, making it harder for nascent flame kernels to attain thermal equilibrium. Experimentally, when the NH_3 fraction in the fuel is raised from 0 % to 20 %, the *MIE* increases from 15.1 mJ to 24.8 mJ, and a further increase from 20 % to 40 % NH_3 lead to an *MIE* of 42.5 mJ. While NH_3 fraction the grows in a linear fashion, the corresponding rise in *MIE* is decidedly nonlinear. To assess the effects of ϕ on ignition behavior, we measured the P_{ig} and *MIE* for 20 %NH_3/80 %C_2H_4/air mixture at $\phi = 0.47$, 0.50, and 0.53, as depicted in Fig. 8 (b). As ϕ decreases, the P_{ig} curves shift progressively to higher energies and the *MIE* rises. This dependency is distinctly nonlinear. A leaner mixture (lower ϕ) releases heat more slowly, so more input energy is required to bring nascent flame kernels to thermal equilibrium and achieve successful ignition. In Fig. 8 (c), the P_{ig} curves for 20 %NH_3/80 %C_2H_4/air mixture are plotted for different flow velocities at V = 7, 10, and 13 m/s. As V increases, the P_{ig} curves shift toward higher energies, indicating that ignition becomes more difficult. Specifically, when V rises from 7 to 13 m/s, the *MIE* nearly doubles (from 17.9 mJ to 34.4 mJ). This trend arises because higher flow velocities intensify flame stretching and convective heat loss. With a Lewis number (*Le*) greater than one, heat diffuses faster than fuel radicals into the reaction zone, causing flame kernels to lose heat and reactive species more quickly than they are replenished. To counter these losses and enable kernel formation and growth, a higher ignition energy is required.

3.3. Analysis of the flame propagation processes

3.3.1. The flame propagation processes of NH_3/air mixture

The effects of nanosecond pulsed discharge excited plasma on ignition and flame propagation were examined by characterizing flame kernels during their quasi-steady state. All experiments were conducted under identical discharge conditions ($f = 20$ kHz, $U_{peak} = 10$ kV, $W = 10$ ns, and $N = 10$). Each data point represents the statistical average of at least ten repeats. Fig. 9 illustrates how the ϕ influences the projected area of NH_3/air flame kernels. As the kernels grow, both their mean area and the scatter about that mean increase: small variations during initial kernel formation amplify over time, producing substantial differences in subsequent growth. As ϕ increases from 0.7 to 0.9, both the kernel area and its growth rate rise, and the curve corresponding to the stoichiometric mixture lies between those for $\phi = 0.7$ and $\phi = 0.8$. One possible explanation is that, as the ϕ increases, the density of the burned gas decreases, thereby increasing the density ratio of unburned to burned gas at the flame front. The enhanced density ratio strengthens the retarding effect on flame propagation and inhibits the growth of the

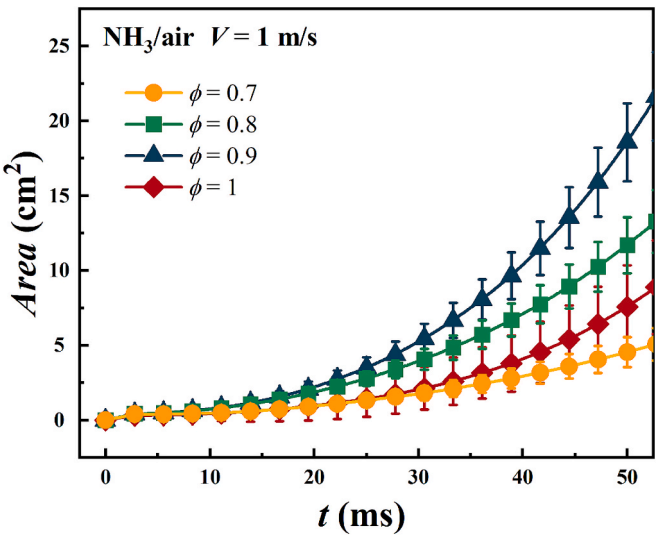

Fig. 9. Variations of the flame area of NH_3/air with time at different equivalence ratios under $V = 1$ m/s.

flame kernels.

The NH_3/air flames exhibit significant self-luminescence when captured by direct-photography. Fig. 10 (a) presents the normalized luminescence intensity (*NLI*) of NH_3/air flames at various ϕ, where each *NLI* curve has been obtained by dividing the instantaneous luminescence intensity by its peak value within the plotting interval. Notably, the stoichiometric flame ($\phi = 1.0$) yields an *NLI* that falls between those for $\phi = 0.8$ and $\phi = 0.9$. At ignition onset, the transient plasma luminescence, generated by electrical breakdown between the electrodes, produces a sharp rise in *NLI* for all mixtures. Beyond $t = 30$ ms, however, the *NLI* of the stoichiometric flame surpasses that of the $\phi = 0.8$ case, despite its smaller kernel size in Fig. 9. This reflects a higher luminescence density in the flame kernel at $\phi = 1$. Fig. 10 (b) depicts the time at which the *NLI* reaches its maximum (NLI_{max}) for NH_3/air flames at various ϕ. All curves have been normalized by dividing each instantaneous *NLI* value by the global maximum *NLI* observed across all test conditions during the process of flame kernel development, ensuring direct comparability between different ϕ. Within the range studied, NLI_{max} increases with ϕ: as ϕ rises from 0.7 to 0.9, the peak occurs progressively earlier. However, when ϕ is increased further from 0.9 to 1.0, the peak arrival is delayed, occurring between the times observed at $\phi = 0.7$ and $\phi = 0.8$, which indicates that the flame kernels reside longer in the combustion chamber at $\phi = 1$.

3.3.2. *The flame propagation processes of NH_3/C_2H_4/air mixture*

The propagation behavior of NH_3/C_2H_4/air flames under high flow velocities was investigated to characterize ignition under highly turbulent conditions. Fig. 11 (a) illustrates the flame kernel area for various fuel compositions at $\phi = 0.5$ and $V = 10$ m/s. The results show that the flame area decreases as the blending ratio of NH_3 increases. This is attributed to the lower chemical reactivity of NH_3, which suppresses flame propagation and consequently hinders the growth of flame kernels at higher NH_3 blending ratios. Fig. 11 (b) depicts the influence of ϕ on the flame kernel area of 20 %NH_3/80 %C_2H_4/air mixtures. In the early stages of flame development, the differences in flame area are minor across different ϕ. As the flame kernels grow, these differences become more pronounced. Similar to the effects of fuel compositions, ϕ exhibits a positive correlation with flame area, indicating that mixtures with higher ϕ possess greater reactivity, which enhances flame propagation and kernel growth. This enhancement is particularly evident during the later stages of flame development. Fig. 11 (c) shows the flame kernel area of a 20 %NH_3/80 %C_2H_4/air mixture over time under different flow velocities at $\phi = 0.5$. During the discharge process, the length of gas exposed to plasma at a fixed electrode gap can be approximated as being positively correlated with the product of discharge duration and flow velocity. The discharge duration is held constant by maintaining fixed discharge parameters. Higher flow velocities result in longer plasma exposure regions, which generate larger initial flame kernels. Meanwhile, the flame kernel area evolves approximately linearly with time across the tested flow velocities, indicating that the flame area growth rates are nearly identical under the present conditions.

3.4. *Characteristics of discharge on flame propagation*

Different discharge parameters also influence the flame propagation process, even though the *MIE* measurements for NH_3/C_2H_4/air flames in this study are conducted under fully coupled conditions [36]. Therefore, this work further investigates the effects of discharge parameters (such as *N* and *f*) on flame propagation. Fig. 12 (a) shows the effect of *N* on the propagation of NH_3/C_2H_4/air flames, with discharge parameters fixed at $U = 13$ kV, $f = 20$ k Hz, and $W = 10$ ns. *N* affects the generation of initial flame kernels by altering energy deposition, and influences the gas exposure duration to plasma by modifying the overall discharge time. As

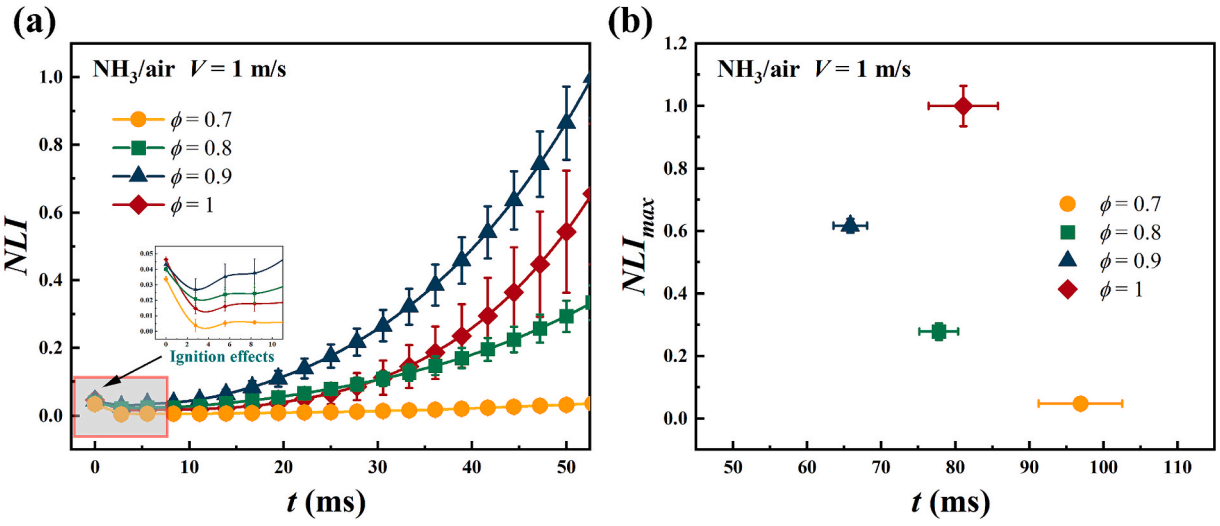

Fig. 10. Variations of the normalized luminous intensity of the NH_3/air flames with time at different equivalence ratios under $V = 1$ m/s. (a) Normalized luminous intensity during the quasi-steady development state; (b) The maximum of normalized luminous intensity throughout the entire flame propagation process.

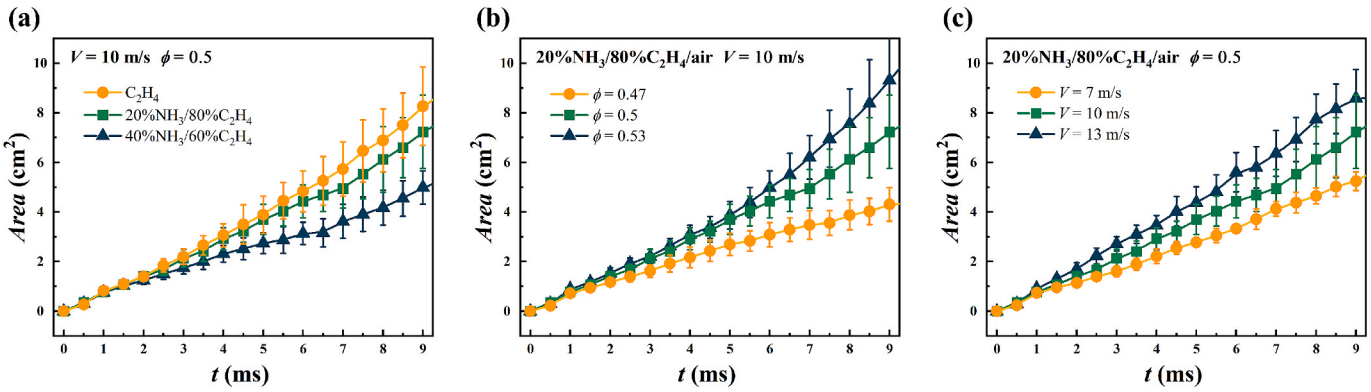

Fig. 11. Variations of the flame area of NH_3/C_2H_4/air mixtures with time under different conditions. (a) Variations of the flame area with time for NH_3/C_2H_4/air flames under $V = 10$ m/s and $\phi = 0.5$ with different fuel compositions; (b) Variations of the flame area with time for 20 %NH_3/80 %C_2H_4/air mixtures under $V = 10$ m/s at different equivalence ratios. (c) Variations of the flame area with time for 20 %NH_3/80 %C_2H_4/air mixtures at $\phi = 0.5$ under different initial flow velocities.

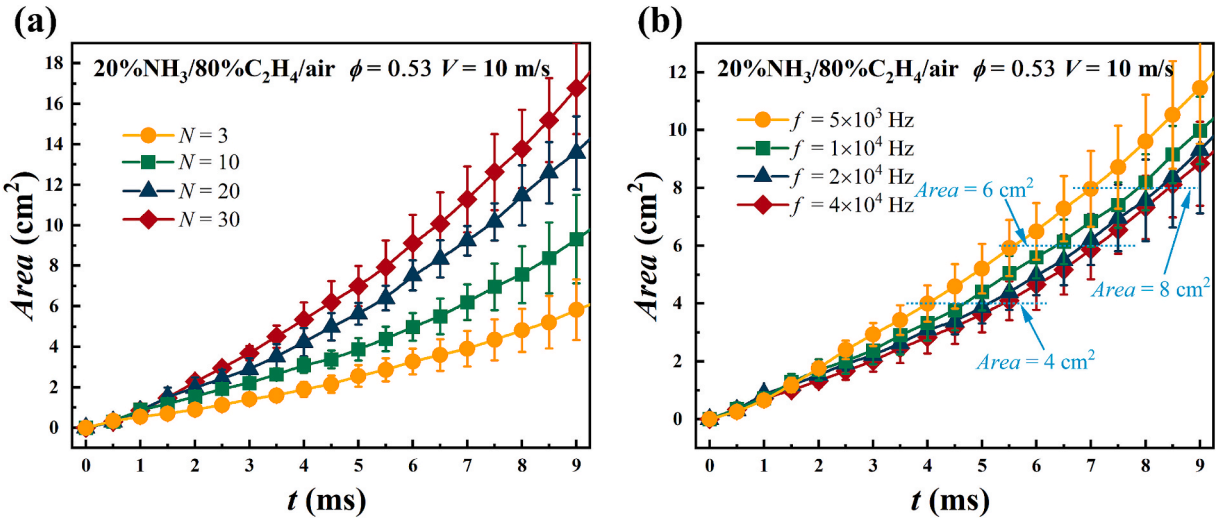

Fig. 12. Variations of the flame area of 20 %NH_3/80 %C_2H_4/air mixtures with time at $V = 10$ m/s and $\phi = 0.53$ under different discharge parameters. (a) Variations of the flame area with time under different number of pulses; (b) Variations of the flame area with time under different discharge frequencies.

time progresses, the flame area increases at all tested N values. However, the area exhibits nonlinear growth with increasing N at the same development time. This behavior is mainly due to greater energy input, extended discharge duration, and a longer plasma exposed gas region at higher N. Nevertheless, beyond a certain threshold, further increases in N do not significantly enhance ignition, suggesting the presence of a saturation point. Under $V = 10$ m/s, NH_3/C_2H_4/air flames remain in a fully coupled state when $f > 5$ k Hz. The f significantly affects flame propagation, as shown in Fig. 12 (b). For this case, the discharge parameters are fixed at $U = 13$ kV, $N = 10$ and $W = 10$ ns. The results reveal that lower frequencies lead to faster flame growth and larger flame areas. This is attributed to the fact that, at the same flow velocity, a lower frequency corresponds to a longer exposure time under plasma, resulting in a larger initial flame kernel, even at constant energy deposition.

To further clarify the effect of f on flame development, Fig. 13 presents the variation in the time required for NH_3/C_2H_4/air flames to reach specific flame areas as a function of f. The relationship between time and f was fitted through an asymptotic nonlinear function:

$$t = a - bc^f \tag{10}$$

where a, b and c were the fitting parameters. It was found that the development time of NH_3/C_2H_4/air flames varied nonlinearly with f for reaching different areas of flames. Reducing f significantly shortened the

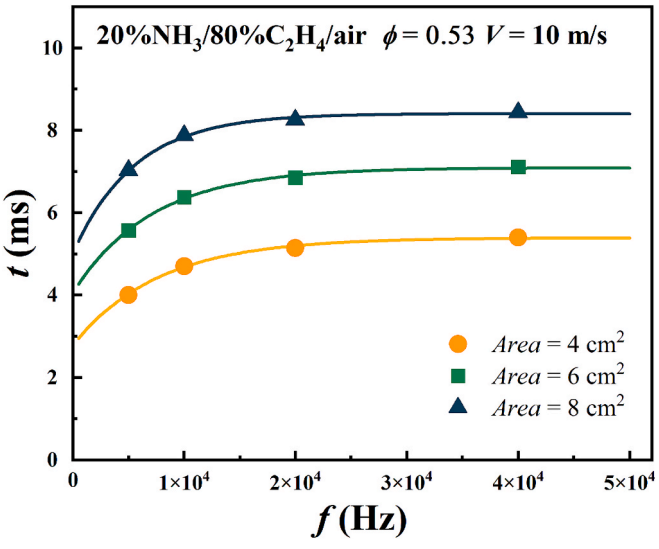

Fig. 13. Variations of the development time of 20 %NH_3/80 %C_2H_4/air flames with discharge frequency for reaching different flame areas at $V = 10$ m/s and $\phi = 0.53$.

time for reaching the target flame area at low f, while the effect was no longer significant at high frequencies.

4. Conclusions

In this study, the ignition and flame propagation characteristics of NH_3/air and NH_3/C_2H_4/air mixtures under flow conditions were systematically investigated using a mini-wind tunnel combustion chamber. The effects of equivalence ratio, fuel composition, flow velocity, and discharge parameters were thoroughly explored. Through high-speed imaging and diagnostic analysis, the ignition and flame propagation characteristics under various conditions were quantitatively characterized. The main results are summarized as follows.

For NH_3/air flames, the *MIE* exhibits a non-monotonic trend with the equivalence ratio, with the lowest *MIE* occurring at an equivalence ratio of approximately 0.85 at lower flow velocities ($V = 1$ m/s). At higher flow velocities ($V > 10$ m/s), the *MIE* of NH_3/C_2H_4/air mixtures increases with lower ϕ, greater NH_3 fractions, and higher V, due to weakened fuel reactivity and enhanced convective losses and flame stretching. The flame propagation process is classified into four distinct stages: (i) ignition stage; (ii) quasi-steady-state development; (iii) the wall-touching propagation; and (iv) outflow. The transition to wall contact accelerates flame expansion, with significantly faster downstream propagation. For NH_3/C_2H_4/air flames, higher V generates larger initial flame kernels due to longer plasma exposure. Moreover, low f and increased N significantly promote flame kernel growth under fully coupled conditions, and the effect of N reaches a saturation point at higher values.

Overall, this work provides fundamental insights into plasma-assisted ignition and flame propagation under flowing conditions for ammonia-containing fuels. The findings contribute to the understanding of low-carbon combustion strategies involving NH_3 and NH_3/hydrocarbon blends. Future work could focus on integrating advanced diagnostics to resolve flame structure and radical generation mechanisms in more detail, aiming to further improve ignition reliability.

CRediT authorship contribution statement

Bowen Liu: Writing – original draft, Methodology, Investigation, Data curation. **Xiaoyang Guo:** Writing – original draft, Methodology, Investigation, Data curation. **Zihao Chen:** Methodology, Investigation. **Erjiang Hu:** Writing – review & editing, Supervision, Project administration, Methodology, Investigation, Conceptualization. **Hao Zhao:** Methodology, Investigation. **Zuohua Huang:** Methodology, Investigation.

Declaration of competing interest

The authors declare that they have no known competing financial interests or personal relationships that could have appeared to influence the work reported in this paper.

Acknowledgements

This study is supported by National Key Research and Development Program of China (2021YFA0716201), the National Natural Science Foundation of China (52176131, 52436004), the Advanced Jet Propulsion Innovation Center Construction (HKCX-2024-01-22), Natural Science Foundation of Shaanxi Province (2023KXJ-228, 2021JLM-18, 2020JC-04), and National Science and Technology Major Project (J2019-III-0004-0047).

Data availability

Data will be made available on request.

References

[1] Yüksel I. Global warming and renewable energy sources for sustainable development in Turkey. Renew Energy 2008;33:802–12. https://doi.org/10.1016/j.renene.2007.05.040.
[2] Sangeeta MS, Pande M, Rani M, Gakhar R, Sharma M, et al. Alternative fuels: an overview of current trends and scope for future. Renew Sustain Energy Rev 2014;32:697–712. https://doi.org/10.1016/j.rser.2014.01.023.
[3] Bao Y, Du H, Chai WS, Nie D, Zhou L. Numerical investigation and optimization on laminar burning velocity of ammonia-based fuels based on GRI3.0 mechanism. Fuel 2022;318:123681. https://doi.org/10.1016/j.fuel.2022.123681.
[4] Ichikawa A, Hayakawa A, Kitagawa Y, Kunkuma Amila Somarathne KD, Kudo T, Kobayashi H. Laminar burning velocity and markstein length of ammonia/hydrogen/air premixed flames at elevated pressures. Int J Hydrogen Energy 2015;40:9570–8. https://doi.org/10.1016/j.ijhydene.2015.04.024.
[5] Ji C, Wang Z, Wang D, Hou R, Zhang T, Wang S. Experimental and numerical study on premixed partially dissociated ammonia mixtures. Part I: laminar burning velocity of $NH_3/H_2/N_2$/air mixtures. Int J Hydrogen Energy 2022;47:4171–84. https://doi.org/10.1016/j.ijhydene.2021.10.269.
[6] Al-Aboosi FY, El-Halwagi MM, Moore M, Nielsen RB. Renewable ammonia as an alternative fuel for the shipping industry. Curr Opin Chem Eng 2021;31:100670. https://doi.org/10.1016/j.coche.2021.100670.
[7] Wang D, Ji C, Wang Z, Wang S, Zhang T, Yang J. Measurement of oxy-ammonia laminar burning velocity at normal and elevated temperatures. Fuel 2020;279:118425. https://doi.org/10.1016/j.fuel.2020.118425.
[8] Mei B, Zhang J, Shi X, Xi Z, Li Y. Enhancement of ammonia combustion with partial fuel cracking strategy: laminar flame propagation and kinetic modeling investigation of $NH_3/H_2/N_2$/air mixtures up to 10 atm. Combust Flame 2021;231:111472. https://doi.org/10.1016/j.combustflame.2021.111472.
[9] Pfahl UJ, Ross MC, Shepherd JE, Pasamehmetoglu KO, Unal C. Flammability limits, ignition energy, and flame speeds in H_2–CH_4–NH_3–N_2O–O_2–N_2 mixtures. Combust Flame 2000;123:140–58. https://doi.org/10.1016/S0010-2180(00)00152-8.
[10] Takizawa K, Takahashi A, Tokuhashi K, Kondo S, Sekiya A. Burning velocity measurements of nitrogen-containing compounds. J Hazard Mater 2008;155:144–52. https://doi.org/10.1016/j.jhazmat.2007.11.089.
[11] Mei B, Zhang X, Ma S, Cui M, Guo H, Cao Z, et al. Experimental and kinetic modeling investigation on the laminar flame propagation of ammonia under oxygen enrichment and elevated pressure conditions. Combust Flame 2019;210:236–46. https://doi.org/10.1016/j.combustflame.2019.08.033.
[12] Okafor EC, Somarathne KDKA, Hayakawa A, Kudo T, Kurata O, Iki N, et al. Towards the development of an efficient low-NOx ammonia combustor for a micro gas turbine. Proc Combust Inst 2019;37:4597–606. https://doi.org/10.1016/j.proci.2018.07.083.
[13] Li H, Xiao H, Sun J. Laminar burning velocity, markstein length, and cellular instability of spherically propagating NH_3/H_2/air premixed flames at moderate pressures. Combust Flame 2022;241:112079. https://doi.org/10.1016/j.combustflame.2022.112079.
[14] Shu T, Xue Y, Zhou Z, Ren Z. An experimental study of laminar ammonia/methane/air premixed flames using expanding spherical flames. Fuel 2021;290:120003. https://doi.org/10.1016/j.fuel.2020.120003.
[15] Liu B, Hu E, Yin G, Huang Z. Experimental and kinetic study on laminar burning velocities of ammonia/ethylene/air premixed flames under high temperature and elevated pressure. Combust Flame 2023;251:112707. https://doi.org/10.1016/j.combustflame.2023.112707.
[16] Yin G, Li J, Zhou M, Li J, Wang C, Hu E, et al. Experimental and kinetic study on laminar flame speeds of ammonia/dimethyl ether/air under high temperature and elevated pressure. Combust Flame 2022;238:111915. https://doi.org/10.1016/j.combustflame.2021.111915.
[17] Issayev G, Giri BR, Elbaz AM, Shrestha KP, Mauss F, Roberts WL, et al. Ignition delay time and laminar flame speed measurements of ammonia blended with dimethyl ether: a promising low carbon fuel blend. Renew Energy 2022;181:1353–70. https://doi.org/10.1016/j.renene.2021.09.117.
[18] Wang Z, Han X, He Y, Zhu R, Zhu Y, Zhou Z, et al. Experimental and kinetic study on the laminar burning velocities of NH_3 mixing with CH_3OH and C_2H_5OH in premixed flames. Combust Flame 2021;229:111392. https://doi.org/10.1016/j.combustflame.2021.02.038.
[19] Lesmana H, Zhu M, Zhang Z, Gao J, Wu J, Zhang D. An experimental investigation into the effect of spark gap and duration on minimum ignition energy of partially dissociated NH3 in air. Combust Flame 2022;241:112053. https://doi.org/10.1016/j.combustflame.2022.112053.
[20] Sadaghiani MS, Arami-Niya A, Zhang D, Tsuji T, Tanaka Y, Seiki Y, et al. Minimum ignition energies and laminar burning velocities of ammonia, HFO-1234yf, HFC-32 and their mixtures with carbon dioxide, HFC-125 and HFC-134a. J Hazard Mater 2021;407:124781. https://doi.org/10.1016/j.jhazmat.2020.124781.
[21] Fernández-Tarrazo E, Gómez-Miguel R, Sánchez-Sanz M. Minimum ignition energy of hydrogen–ammonia blends in air. Fuel 2023;337:127128. https://doi.org/10.1016/j.fuel.2022.127128.
[22] Yu C, Eckart S, Essmann S, Markus D, Valera-Medina A, Schießl R, et al. Investigation of spark ignition processes of laminar strained premixed stoichiometric NH3-H2-air flames. J Loss Prev Process Ind 2023;83:105043. https://doi.org/10.1016/j.jlp.2023.105043.
[23] Chen Z, Burke MP, Ju Y. On the critical flame radius and minimum ignition energy for spherical flame initiation. Proc Combust Inst 2011;33:1219–26. https://doi.org/10.1016/j.proci.2010.05.005.

[24] Kim HH, Won SH, Santner J, Chen Z, Ju Y. Measurements of the critical initiation radius and unsteady propagation of *n*-decane/air premixed flames. Proc Combust Inst 2013;34:929–36. https://doi.org/10.1016/j.proci.2012.07.035.
[25] Verkamp FJ, Hardin MC, Williams JR. Ammonia combustion properties and performance in gas-turbine burners. Symp (Int) Combust 1967;11:985–92. https://doi.org/10.1016/S0082-0784(67)80225-X.
[26] Lefkowitz JK, Ombrello T. Reduction of flame development time in nanosecond pulsed high frequency discharge ignition of flowing mixtures. Combust Flame 2018;193:471–80. https://doi.org/10.1016/j.combustflame.2018.04.009.
[27] Lovascio S, Ombrello T, Hayashi J, Stepanyan S, Xu D, Stancu GD, et al. Effects of pulsation frequency and energy deposition on ignition using nanosecond repetitively pulsed discharges. Proc Combust Inst 2017;36:4079–86. https://doi.org/10.1016/j.proci.2016.07.065.
[28] Mao X, Zhong H, Wang Z, Ombrello T, Ju Y. Effects of inter-pulse coupling on nanosecond pulsed high frequency discharge ignition in a flowing mixture. Proc Combust Inst 2023;39:5457–64. https://doi.org/10.1016/j.proci.2022.06.018.
[29] Opacich KC, Heyne JS, Gray JAT, Busby K, Hammack SD, Ombrello T. Ignition kernel development in a reactive flow for nanosecond-pulsed high-frequency and DC arc discharges. Combust Flame 2022;245:112324. https://doi.org/10.1016/j.combustflame.2022.112324.
[30] Opacich KC, Ombrello TM, Heyne JS, Lefkowitz JK, Leiweke RJ, Busby K. Analyzing the ignition differences between conventional spark discharges and nanosecond-pulsed high-frequency discharges. Proc Combust Inst 2021;38:6615–22. https://doi.org/10.1016/j.proci.2020.06.322.
[31] Adams S, Miles J, Ombrello T, Brayfield R, Lefkowitz J. The effect of inter-pulse coupling on gas temperature in nanosecond-pulsed high-frequency discharges. J Phys D Appl Phys 2019;52:355203. https://doi.org/10.1088/1361-6463/ab27ef.
[32] Lin B, Wu Y, Zhang Z, Chen Z. Multi-channel nanosecond discharge plasma ignition of premixed propane/air under normal and sub-atmospheric pressures. Combust Flame 2017;182:102–13. https://doi.org/10.1016/j.combustflame.2017.04.022.
[33] Pai DZ, Lacoste DA, Laux CO. Nanosecond repetitively pulsed discharges in air at atmospheric pressure—the spark regime. Plasma Sources Sci Technol 2010;19:65015. https://doi.org/10.1088/0963-0252/19/6/065015.
[34] Starikovskaia S. Plasma-assisted ignition and combustion: nanosecond discharges and development of kinetic mechanisms (34 pp) J Phys D Appl Phys 2014;47:353001. https://doi.org/10.1088/0022-3727/47/35/353001.
[35] Bonebrake JM, Blunck DL, Lefkowitz JK, Ombrello TM. The effect of nanosecond pulsed high frequency discharges on the temperature evolution of ignition kernels. Proc Combust Inst 2019;37:5561–8. https://doi.org/10.1016/j.proci.2018.06.027.
[36] Lefkowitz JK, Ombrello T. An exploration of inter-pulse coupling in nanosecond pulsed high frequency discharge ignition. Combust Flame 2017;180:136–47. https://doi.org/10.1016/j.combustflame.2017.02.032.
[37] Choe J, Sun W, Ombrello T, Carter C. Plasma assisted ammonia combustion: simultaneous NOx reduction and flame enhancement. Combust Flame 2021;228:430–2. https://doi.org/10.1016/j.combustflame.2021.02.016.
[38] Zhang B, Rubio M, Egolfopoulos F, Cronin SB. Stable combustion of ammonia in an internal combustion engine: a single fuel approach enabled by multi-pulse transient plasma ignition. Fuel 2025;381:133502. https://doi.org/10.1016/j.fuel.2024.133502.
[39] Wang S, Wei X, Gu M, Lin Q, Luo G, Hu F. Flame characteristics and NO emission law of sliding arc plasma-assisted ammonia combustion. Combust Flame 2025;274:114000. https://doi.org/10.1016/j.combustflame.2025.114000.
[40] Do H, Im S, Cappelli MA, Mungal MG. Plasma assisted flame ignition of supersonic flows over a flat wall. Combust Flame 2010;157:2298–305. https://doi.org/10.1016/j.combustflame.2010.07.006.
[41] Do H, Cappelli MA, Mungal MG. Plasma assisted cavity flame ignition in supersonic flows. Combust Flame 2010;157:1783–94. https://doi.org/10.1016/j.combustflame.2010.03.009.
[42] Ombrello TM, Hammack SD, Carter CD, Busby K, Lefkowitz JK. Scramjet cavity ignition using nanosecond-pulsed high-frequency discharges. Combust Flame 2024;262:113335. https://doi.org/10.1016/j.combustflame.2024.113335.
[43] Rudz S, Tadini P, Berthet F, Gillard P. Effect of low initial pressures on ignition properties of lean and rich n-decane/air mixtures for laser-induced breakdown. Combust Sci Technol 2019;191:223–42.
[44] Eckhoff RK, Ngo M, Olsen W. On the minimum ignition energy (MIE) for propane/air. J Hazard Mater 2010;175:293–7. https://doi.org/10.1016/j.jhazmat.2009.09.162.